ADVANCED INTELLIGENT SYSTEMS Open Access
www.advintellsyst.com

Biopolymer Cryogels for Transient Ecology-Drones

Fabian Wiesemüller, Severin Meyer, Yijie Hu, Dominik Bachmann, Annapaola Parrilli, Gustav Nyström, and Mirko Kovač**

Aerial robots can autonomously collect temporal and spatial high-resolution environmental data. This data can be utilized to develop mathematical ecology models to understand the impact of climate change on the habitat. In case of drone malfunction, the incorporated materials can threaten vulnerable environments. The recent introduction of transient robotics enables the development of biodegradable, environmental-sensing drones capable of degrading in their environment. However, manufacturing methods for environmental-sensing transient drones are rarely discussed. Herein, a manufacturing framework and material selection process featuring biopolymer-based, high-strength composite cryogels, and printed carbon-based electronics for transient drones are highlighted. It is found that gelatin- and cellulose-based cryogels mechanically outperform other biopolymer composites while having a homogeneous microstructure and high stiffness-to-weight ratio. The selected materials are used to manufacture a flying-wing air-frame, while the incorporated sensing skin is capable of measuring the elevons' deflection angles as well as ambient temperature. It is demonstrated in the results how gelatin–cellulose cryogels can be used to manufacture lightweight transient drones, while printing carbon-conductive electronics is a viable method for designing sustainable, integrated sensors. The proposed methods can be used to guide the development of lightweight and rapidly degrading robots, featuring eco-friendly sensing capabilities. An interactive preprint version of the article can be found here: https://doi.org/10.22541/au.167506513.33779420/v1.

1. Introduction

Natural forests are one of the world's largest carbon sinks, absorbing approximately two billion tonnes of CO_2 per year.[1,2] To improve understanding of forest ecosystems and develop conservation strategies, more sophisticated energy balance models need to be developed.[3] Research activities must focus on understanding changes in the vegetative phenology and the ecosystem energy or mass exchanges, which influence the ecosystem carbon production and productivity levels.[4–6]

Many factors need to be studied and modeled to estimate CO_2 budgets[7] and guide policymakers and environmentalists toward efficient strategies for carbon sequestration in forests.[8] To develop these models, environmental data with high temporal and spatial resolution is of the utmost importance. This requires time-consuming, complex, and expensive methods to manually distribute build-to-last sensing devices with human workers.[9] These sensing devices still pose a threat to the environment in which they are deployed in, as they are nondegradable and potentially toxic.

F. Wiesemüller, S. Meyer, M. Kovač
Laboratory of Sustainability Robotics
Empa - Swiss Federal Laboratories for Materials Science and Technology
8600 Dübendorf, Switzerland
E-mail: fabian.wiesemueller@empa.ch; m.kovac@imperial.ac.uk

F. Wiesemüller, S. Meyer, M. Kovač
Aerial Robotics Laboratory
Imperial College London, South Kensington Campus
London SW7 2AZ, UK

Y. Hu, G. Nyström
Laboratory for Cellulose & Wood Materials
Empa - Swiss Federal Laboratories for Materials Science and Technology
8600 Dübendorf, Switzerland

The ORCID identification number(s) for the author(s) of this article can be found under https://doi.org/10.1002/aisy.202300037.

© 2023 The Authors. Advanced Intelligent Systems published by Wiley-VCH GmbH. This is an open access article under the terms of the Creative Commons Attribution License, which permits use, distribution and reproduction in any medium, provided the original work is properly cited.

DOI: 10.1002/aisy.202300037

Y. Hu
State Key Laboratory of Pulp and Paper Engineering
South China University of Technology
Guangzhou 510640, China

D. Bachmann
Transport at Nanoscale Interfaces Laboratory
Empa - Swiss Federal Laboratories for Materials Science and Technology
8600 Dübendorf, Switzerland

G. Nyström
Department of Health Sciences and Technology
ETH Zürich
8092 Zürich, Switzerland

A. Parrilli
Center for X-ray Analytics
Empa - Swiss Federal Laboratories for Materials Science and Technology
8600 Dübendorf, Switzerland

Alternatively, robotic platforms can be utilized to automatize data sampling while reducing risks and costs.[10,11] If drone control is lost, its structure and active components could pollute and harm the environment, making e-waste recovery critical. This may be challenging for hard-to-reach and sensitive environments. Therefore, drone capabilities for autonomous environmental sensing of sensitive environments are limited.

To enable autonomous, robotic, and eco-friendly environmental monitoring, transient robotic devices need to be manufactured purely from biodegradable and nonfossil-based materials.[12,13] These transient drones[12,14,15] are designed to collect, store, and transmit environmental data by reaching difficult to access locations through flight. Due to the biodegradability of their active and passive components,[16–18] these systems do not need to be recovered and can be left for degradation, where nutritional sources contained in their components are directly fed back into the biomass energy cycle. This eco-friendly approach to joint material and system development[19,20] for environmental monitoring is a viable alternative to traditional robotic systems designed for monitoring and manipulating the environment. **Figure 1** shows a conceptual illustration of the herein proposed transient drone deployed in a tropical environment.

To develop lightweight but structurally high-performing transient drones, materials that feature superior mechanical properties, inherent sustainability, and biodegradability need to be engineered. Cellulose is a natural biopolymer composed of $\beta-(1 \rightarrow 4)$-linked d-glucose units with an annual synthesis of 75 billion tons,[21] which makes it the most abundant polymer on earth. Its superior mechanical properties, inherent biodegradability and the possibility for functionalization[22,23] make it an ideal candidate for designing systems that can combine structural integrity, sensing capabilities, and eco-friendliness. For manufacturing a structurally efficient flying drone, the specific stiffness and specific strength of the structure need to be maximized. Since the bulk densities of cellulose and other biopolymers are too high, they do not qualify for a lightweight unmanned aerial drone. Cryogels or aerogels are lightweight material systems with good mechanical properties, featuring a porosity higher than 95% and 99%,[24] respectively. Cryogels are prepared through the lyophilization of frozen gels, while aerogels are generally prepared through supercritical drying.[25] Considering cellulose's low cost, wide availability, and biodegradability, it is an ideal raw material for cryogel or aerogel preparation. To achieve a larger surface area as well as better mechanical properties, the cellulose is fibrillated, resulting in micro-fibrillated cellulose (MFC), a 3D network of microfibrils. Nevertheless, most cellulose-based foams show low mechanical strength, which is fatal for withstanding dynamic forces acting on the structure in-flight.[26–28] The most effective way to improve the mechanical strength of cellulose-based foams is to enhance their networks by introducing polymers or nanofillers. For example, Fu et al. interconnected cellulose/boron nitride nanosheet skeletons with epichlorohydrin and polyethylene glycol via self-assembly, vacuum impregnation, and cold compressing and displayed a compressive strength of 3.03 MPa.[29] Liu et al. prepared a ternary material system based on polyvinyl alcohol, montmorillonite clay platelets, and cellulose nanofibrils with a yield strength of 250 kPa and 95% porosity. In situ chemical cross-linking using borax dramatically changed the cellular structure and improved its strength to almost 900 kPa.[30] However, these methods usually involve toxic as well as fossil materials and complex preparation processes.

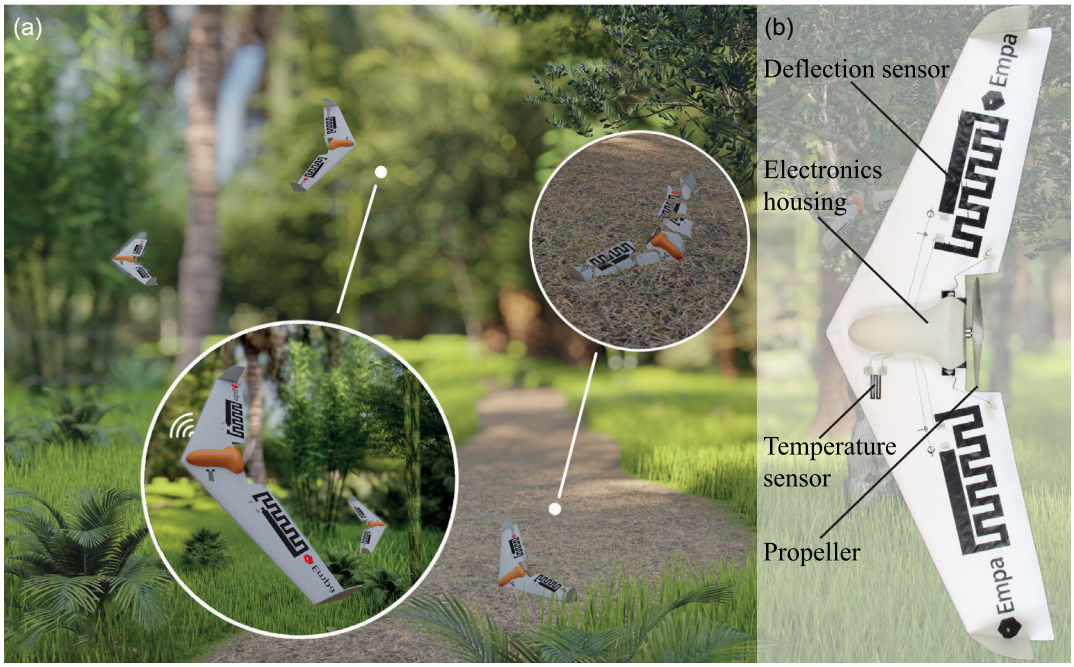

Figure 1. Developed transient drone for environmental monitoring. a) Conceptual illustration of the transient drone in a tropical environment. After the collection and transmission of environmental data, the drone crashes, and the structures degrade. Only the electronics compartment painted in highly visible colors remains and needs to be picked up by a field worker. b) Photograph of the final transient prototype indicating the main components.

© 2023 The Authors. Advanced Intelligent Systems published by Wiley-VCH GmbH

26404567, 2023, 7, Downloaded from https://onlinelibrary.wiley.com/doi/10.1002/aisy.202300037 by Imperial College London, Wiley Online Library on [02/08/2023]. See the Terms and Conditions (https://onlinelibrary.wiley.com/terms-and-conditions) on Wiley Online Library for rules of use; OA articles are governed by the applicable Creative Commons License

In this work, we introduce gelatin to form a cross-linked network with MFC to manufacture high-strength environmentally friendly structures, while comparing it to starch and agar MFC composites. Gelatin is a collection of peptides and proteins produced by partial hydrolysis of collagen extracted from the skin, bones, and connective tissues of animals. It can form cross-linked networks through sol–gel process. Via the composition of gelatin and MFC, the cross-linked porous structure can effectively transfer stress, leading to a high-strength cryogel with a strength of up to 542 kPa and a modulus of 12 000 kPa. The developed material systems are utilized to manufacture the lightweight and biodegradable air-frame of a transient drone and combined with eco-friendly sensors, enabling proprioceptive and exteroceptive monitoring capabilities. To realize full functionality, traditional electronics were incorporated into an electronics housing, prohibiting the contamination of the environment with toxic components.

2. Fabrication

In this section, the manufacturing methods for generating the lightweight structures and the sensing skin of the proposed transient drone concept are presented. The foams were manufactured through lyophilization of MFC and biopolymer solutions or suspensions. The sensing skin was prepared from carbon-conductive ink printed on low-roughness cellulose paper using inkjet printing.

2.1. Material Development

For the preparation of all cryogel composites, MFC was used and mixed with starch, agar, and gelatin. The manufacturing and characterization of the used MFC were performed according to our previous work.[31–33] As a summary, an ultrafine friction grinder supermass colloider (MKZA10-20J CE, Masuko Sangyo Co., Ltd., Kawaguchi/Saitama, Japan) with a grinding energy input of 9 kWh kg^{-1} (referred to dry MFC content) was used to ground aqueous Eucalyptus pulp suspension at an initial concentration of 2 wt%. To reach a solid content of about 11.6 wt%, the MFC suspension was dewatered with a sieve under pressure. Lignin and hemicellulose were removed by the producer through bleaching the slurry. No chemical treatment (e.g., oxidation) was performed on the cellulose pulp before mechanical disintegration. For investigating the structural performance of different material combinations, a sweep over various weight contents ranging from 1% to 8% total solid content was performed. The biopolymers starch, agar, and gelatin were mixed at a 1:1 weight content ratio with MFC. For comparison, cryogels were prepared from the plain biopolymers MFC, starch, agar, and gelatin. An overview of all the material combinations, their cryogel mass ratios and the total and individual solid content in the aqueous slurry is given in Table S1 in Section 1.3.1 in Supporting Information.

All the cryogels were prepared following the same manufacturing steps. Varying amounts of MFC at 11.6 wt% were filled into a beaker and diluted to the required weight content using deionized water. After closing the beaker using a glass plate, the MFC was homogenized using a magnetic stirrer and heated to 40 °C. In parallel, the chosen amount of starch (Sobocat HC, Südstärke GmbH, Schrobenhausen, Germany), agar (Agar Powder, Dixa AG, St. Gallen, Switzerland), or gelatin (Gelatin from porcine skin, G2500, Sigma–Aldrich/Merck KGaA, Darmstadt, Germany) was dissolved in deionized water at 40 °C for starch and gelatin and 100 °C for agar. Afterward, the MFC and biopolymer slurries were mixed together and stirred until homogenized. The gel-like slurry was poured into a 150 × 150 mm (internal dimensions) wide fused deposition modeling (FDM) printed mold, which consisted of a lower lid and an 11 mm high spacer screwed to it. After the slurry was spread uniformly, the upper lid was placed on top and fixed in place by tightening it using screws. The closed mold was precooled in a fridge at 4 °C for at least 8 h and subsequently placed in a freezer (TUS 80–100 LOGG, FRYKA-Kältetechnik GmbH, Esslingen, Germany) at −80 °C for at least 24 h. Afterward, the mold was taken out of the freezer, and the upper and lower lids were replaced with a lid featuring 225 5 mm diameter holes to enable evaporation. The still frozen mold and specimen were placed on the metal racks in the glass chamber of a laboratory freeze-dryer (Alpha 3-4 LSCbasic, Martin Christ Gefriertrocknungsanlagen GmbH, Osterode, Germany) and freeze-dried for at least 72 h at a pressure of 0.05 mbar. All cryogels exhibited a volumetric shrinkage of less than 5%. After drying, the plates were removed from the molds and cut into the required shapes using a laser cutter (Nova24 60W, Thunder Laser Tech Co., Ltd., Shatian, China). Furthermore, an FDM-printed grinding jig featuring sanding paper was used to manually grind the height of the samples to the required dimensions. An overview of the manufacturing process is given in **Figure 2**a.

2.2. Printed Sensors

To enable proprioceptive and environmental sensing capabilities at a low environmental impact, the sensors were printed from a carbon-black-based conductive ink. To achieve rapid prototyping iteration cycles, low-cost manufacturing and full control over the printed geometry, inkjet printing was selected. A commercial inkjet printer (ET-1170, Seiko Epson Corporation, Tokyo, Japan) featuring a refillable ink-storage tank was chosen to enable testing of various conductive inks. The proposed sensing skin was printed using carbon-black nanoparticle ink (JR-700LV, NovaCentrix, Austin, USA) on low-roughness electronics paper substrate (PowerCoat XD 80, Arjowiggins Ltd., Aberdeen, UK). It was found that the structures printed at the highest volumetric deposition setting did not achieve the anticipated conductivity. To mitigate this, several layers of deposited ink were printed on the substrate. Analyzing the conductivity depending on the number of passes showed that a minimum resistivity was achieved at three consecutive passes. Various curing methods (thermal-, UV-, and air-curing) of the printed structures were investigated. The tests conducted showed that air-curing resulted in the lowest resistivity, nevertheless requiring the longest drying time. To speed up the drying process, the printed structures were placed on a heating pad set to 40 °C. A resistance of 7.3 kΩ per square was achieved. The printing process is summarized in Figure 2b.

To achieve real-time information on the position of the elevons of the flying wing, printed bending sensors were embedded

© 2023 The Authors. Advanced Intelligent Systems published by Wiley-VCH GmbH

26404567, 2023, 7, Downloaded from https://onlinelibrary.wiley.com/doi/10.1002/aisy.202300037 by Imperial College London, Wiley Online Library on [02/08/2023]. See the Terms and Conditions (https://onlinelibrary.wiley.com/terms-and-conditions) on Wiley Online Library for rules of use; OA articles are governed by the applicable Creative Commons License

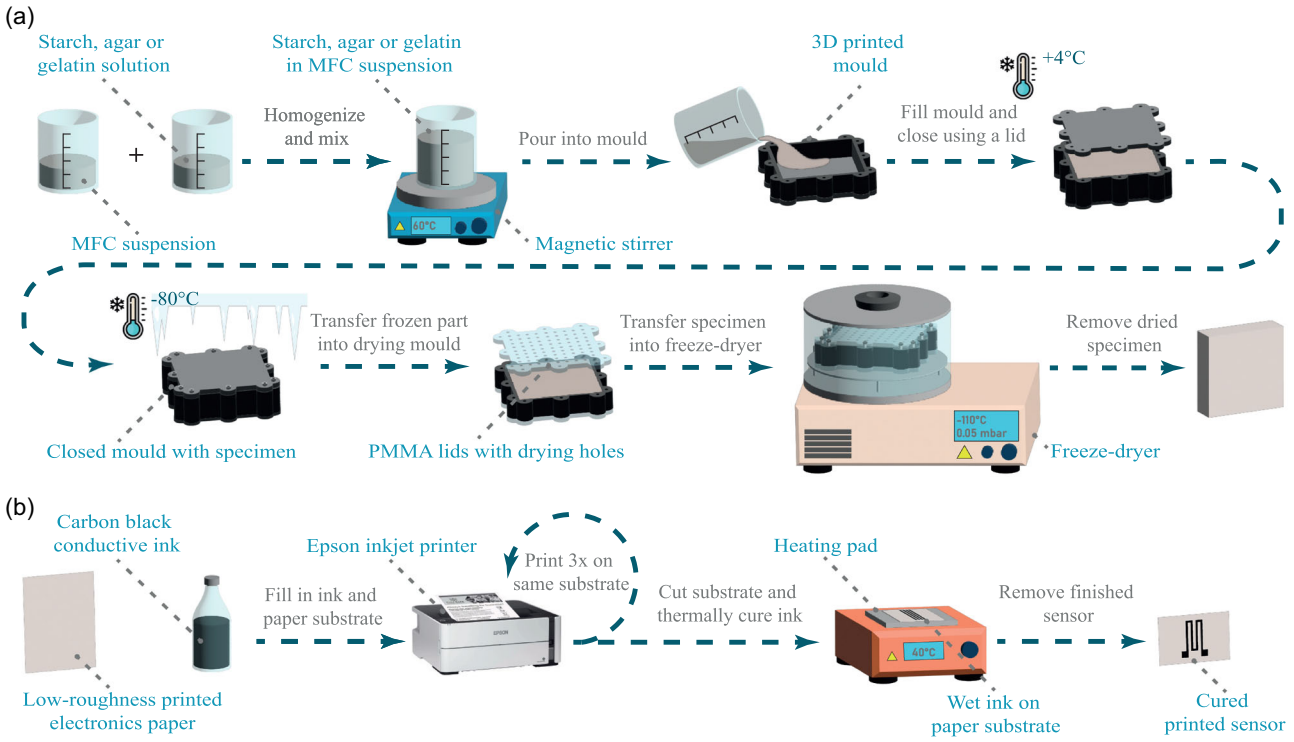

Figure 2. Manufacturing process flowchart. a) For the cryogel air-frame, the micro-fibrillated cellulose (MFC) suspension and the starch, agar, or gelatin solution are homogenized using a magnetic stirrer, and the slurry is poured into a 3D-printed square mold. The mold is closed and placed in a refrigerator. After 8 h, the specimen is transferred into a −80 °C freezer overnight. Afterward, the lids are swapped with poly(methyl methacrylate) (PMMA) lids featuring drying holes and the assembly is placed in a freeze drier for at least 72 h. The finished specimen is removed and cut into the desired size using a laser cutter. b) Sensing skin-manufacturing process flowchart. The low-roughness electronics paper was placed in the paper tray of the printer. Afterward, the carbon-conductive ink was printed three times at the same locations. The wet sensor was then cured using a heating pad.

onto the wing. The sensors were placed on the deflecting section of the elevon spanning half of the wingspan. The final sensor was designed to feature 438 kΩ of total resistance, which corresponds to 60 squares with the given sheet resistance. For each elevon, one of the sensors was utilized. For collecting environmental data such as the ambient temperature, another sensor was printed on the paper substrate at the fuselage section of the wing. For realizing the temperature sensor, a 500 kΩ resistor (16 mm long and 9 mm wide) was chosen and coated using beeswax. Both resistive sensors were connected via zinc wires with a custom-developed sensor terminal, located on the fuselage section. An overview of the sensor layout and the integrated flying wing demonstrator is given in **Figure 3**. Details of the fabrication of the flying wing demonstrator are given in Supporting Information 1.1.1.

3. Results and Discussion

In this section, the mechanical properties of the cryogels are summarized and the microstructure based on scanning electron microscopy (SEM) images and μ-computer tomography (μ-CT) scans are characterized. Furthermore, the biodegradation of the investigated materials is quantified and the performance of the sensing skin is investigated. At the end, the drone testing results are presented.

3.1. Cryogel Mechanical Properties

The mechanical properties of the manufactured samples were evaluated through compression tests using a mechanical testing machine (Z100 AllroundLine, ZwickRoell GmbH & Co. KG, Ulm, Germany) in combination with a 1 kN load-cell and two 160 mm diameter circular compression plates made from steel. For calculating the compressive modulus E_c as well as the compressive strength σ_c, the tests were performed on the basis of ASTM D1621.[34] A minimum of three 35 × 35 mm large square samples were cut from the 11 mm thick cryogel plates using a CO_2 laser cutter (Nova24 60W, Thunder Laser Tech Co., Ltd., Shatian, China) operated at 75% power and 30 mm s^{-1} cutting speed. The samples were then ground to a nominal thickness of 10 mm using a custom 3D-printed grinding jig. The samples were placed in the center of the compression plates and compressed at a rate of 1 mm min^{-1}. The apparent modulus and the strength based on 10% deformation were calculated using a MATLAB (The MathWorks, Inc., Natick, Massachusetts, USA) script. To calculate the specific compressive stiffness as well as the specific compressive strength, the individual sample masses were detected using a precision balance (Kern PCB 250-3, KERN & SOHN GmbH, Balingen-Frommern, Germany). **Figure 4**a summarizes the specific stiffness in kPa g^{-1} cm^3 of the composite–cryogels made from MFC with starch, agar, or

© 2023 The Authors. Advanced Intelligent Systems published by Wiley-VCH GmbH

26404567, 2023, 7, Downloaded from https://onlinelibrary.wiley.com/doi/10.1002/aisy.202300037 by Imperial College London, Wiley Online Library on [02/08/2023]. See the Terms and Conditions (https://onlinelibrary.wiley.com/terms-and-conditions) on Wiley Online Library for rules of use; OA articles are governed by the applicable Creative Commons License

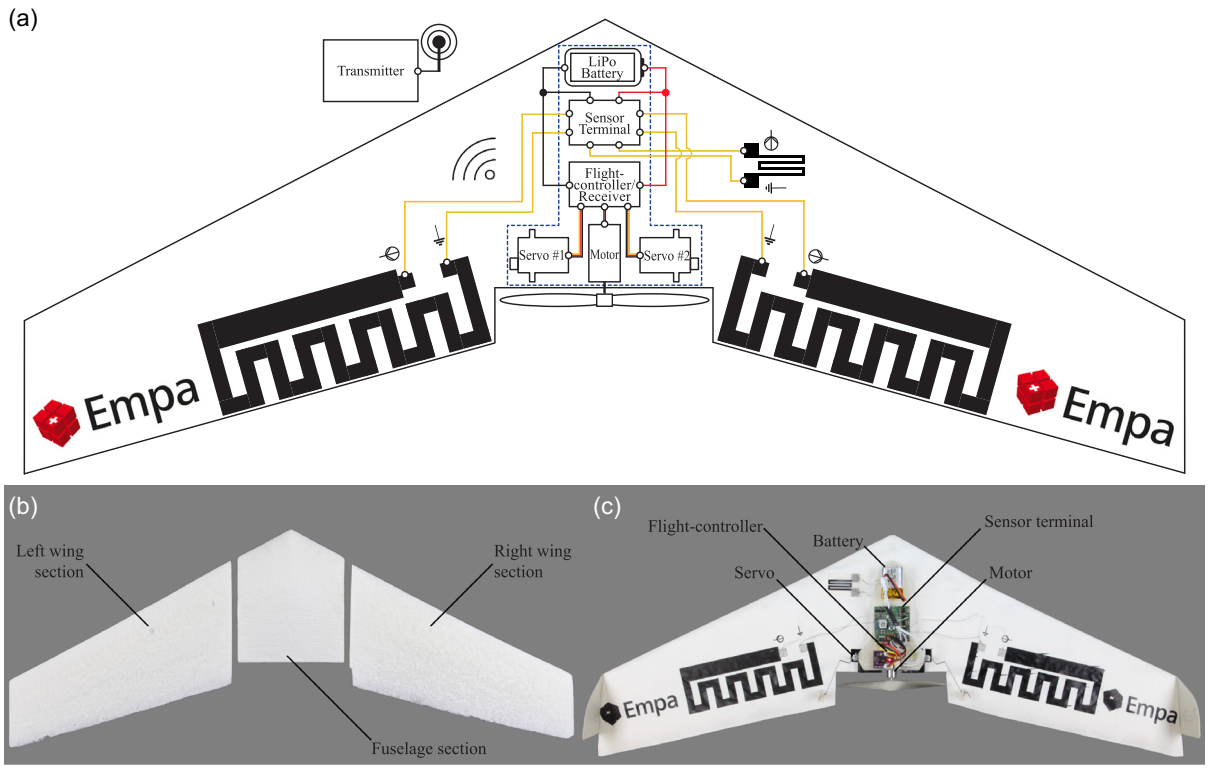

Figure 3. Overview of the drone. a) System–architecture overview of the transient drone indicating the proprioception and exteroceptive sensor layout integrated on the sensing skin. The deflection sensors are located on each wing close to the trailing edge, while the temperature sensor is located on the fuselage section. The battery, the sensor terminal, the flight controller/receiver, the motor, and the servo motors are indicated. The components mounted to the electronics housing are indicated with a dashed blue line. b) Cryogel cores before bonding the wing sections to the fuselage section. c) Finished drone with the electronics mounted to the housing and the sensors connected with the sensor terminal. For better representation, the hood is not closed in this photograph.

gelatin, while Figure 4b gives the specific strength in kPa g^{-1} cm^3 of the same cryogels. Figure 4c summarizes the specific stiffness in kPa g^{-1} cm^3 of the plain cryogels made from a 6 wt% slurry or suspension of MFC, starch, agar, and gelatin, while Figure 4d gives the values of the specific strength in kPa g^{-1} cm^3 for the same cryogels. For comparison the specific stiffness of the 6% MFC:G has a specific stiffness of 10.39×10^4 kPa g^{-1} cm^3 ($s = \pm 3.07 \times 10^4$ kPa g^{-1} cm^3) and a specific strength of 4 754 kPa g^{-1} cm^3 ($s = \pm 848$ kPa g^{-1} cm^3).

To model the mechanical properties of the foams depending on the relative density, Gibson and Ashby's[35] cellular solids model was deployed. According to them, the porosity of a foam P is given by Equation (1), where ρ^*/ρ_s corresponds to the relative density, which is expressed as the density of the foam ρ^* divided by the density of the cell wall material ρ_s. The densities of the cell wall material were calculated using the rule of mixture. Doing so, the two phases n and their respective weight fraction w_i were used to calculate ρ_s

$$P = 1 - \frac{\rho^*}{\rho_s}, \quad \frac{1}{\rho_s} = \sum_{n=1}^{n} \frac{w_i}{\rho_i} \tag{1}$$

An overview of the densities of the measured foams, the computed cell wall material densities as well as the calculated average porosities of the foams are given in Table S2 in Section 1.3.2 in Supporting Information. Note that the values for MFC:S at 1 wt% total and MFC:G at 1 wt% total are not given. The foams collapsed during handling and therefore no reliable data was measured. The standard deviation for each value is given in brackets. According to Gibson and Ashby,[35] the scaling laws of the Young's modulus and strength for open cell foams are given by Equation (2), where E_s is the modulus of the solid cell wall material and E^* is the modulus of the foam, while σ_s and σ^* correspond to the yield strength of the solid cell wall material and the compressive strength of the foam

$$\frac{E^*}{E_s} = \left(\frac{\rho^*}{\rho_s}\right)^2, \quad \frac{\sigma^*}{\sigma_s} = 0.3\left(\frac{\rho^*}{\rho_s}\right)^{\frac{3}{2}} \tag{2}$$

For estimating E_s and σ_s, the measured values of E^* and σ^* in relation to the relative density (ρ^*/ρ_s) were plotted in Figure S1a, b, respectively, in Section 1.2.1 in Supporting Information. Fitting polynomial regressions to the power of 2 for the Young's modulus and to the power of 3/2 for the strength, the acquired data can be used to calculate E_s and σ_s. The determined values for the stiffness and strength are provided in Supporting Information in Table S2 in Section 1.3.2. For MFC:S, a stiffness of 494.1 MPa and a strength of 23.61 MPa; for MFC:A, a stiffness of 150.4 MPa and strength of 12.05 MPa;

© 2023 The Authors. Advanced Intelligent Systems published by Wiley-VCH GmbH

26404567, 2023, 7, Downloaded from https://onlinelibrary.wiley.com/doi/10.1002/aisy.202300037 by Imperial College London, Wiley Online Library on [02/08/2023]. See the Terms and Conditions (https://onlinelibrary.wiley.com/terms-and-conditions) on Wiley Online Library for rules of use; OA articles are governed by the applicable Creative Commons License

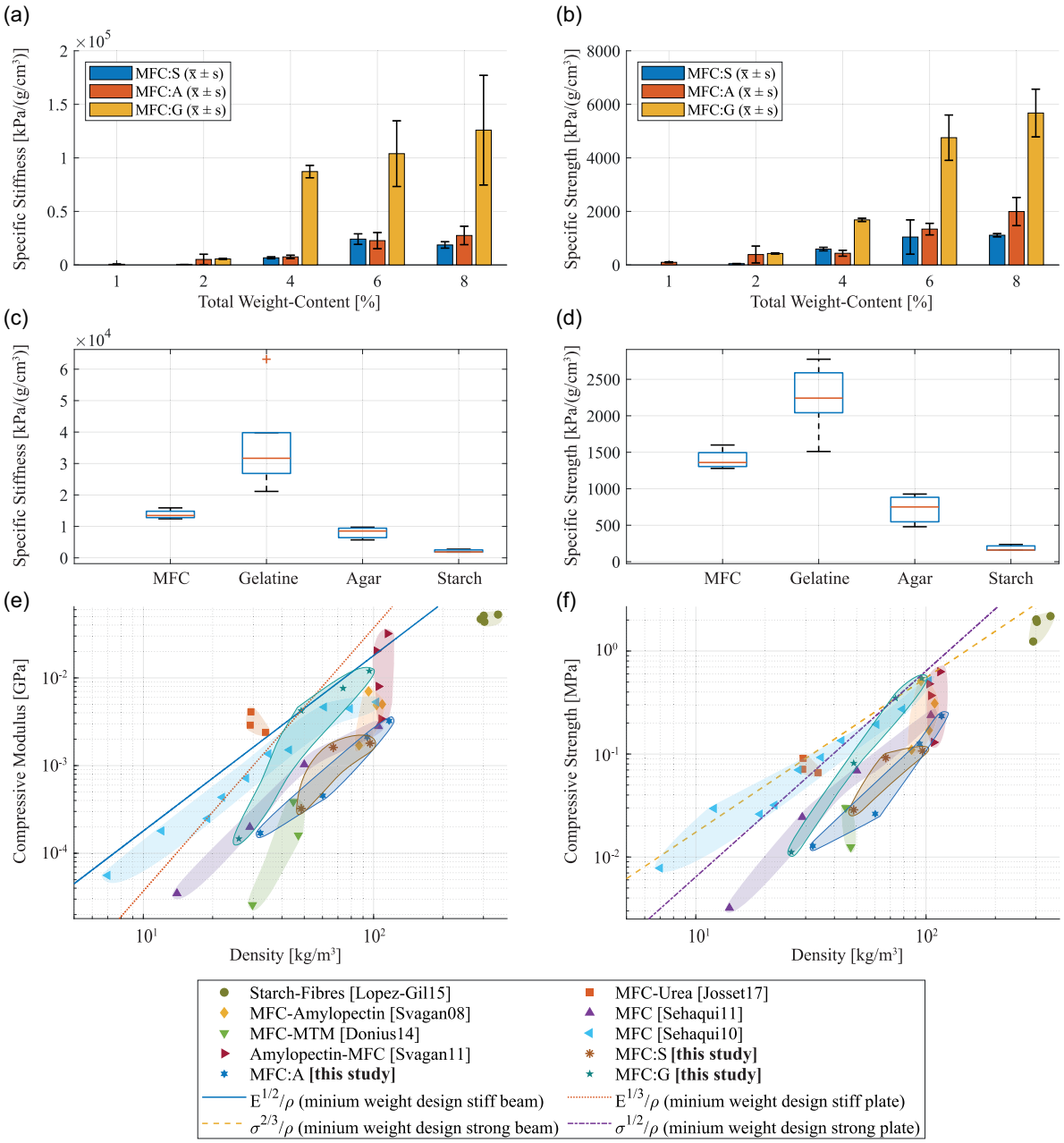

Figure 4. Overview of the mechanical properties of the investigated biopolymer cryogels. The mean values and the standard deviations are given as well as two Ashby plots comparing the properties of other isotropic, biodegradable, and nonfossil foams[24,32,54–58] are given. a) Specific stiffness in kPa g^{-1} cm^3 of the MFC:S, MFC:A, and MFC:G cryogels at 1%, 2%, 4%, 6%, and 8% weight content. b) Specific strength in kPa g^{-1} cm^3 of the MFC:S, MFC:A, and MFC:G cryogels at 1%, 2%, 4%, 6%, and 8% weight content. c) Specific stiffness in kPa g^{-1} cm^3 of the plain cryogels at a total weight content of 6%. d) Specific strength in kPa g^{-1} cm^3 of the plain cryogels at a total weight content of 6%. e) Ashby plot giving the compressive modulus versus the density of the starch, agar, and gelatin composites and comparing it with other materials. The guidelines for minimum weight design of stiff beams and of stiff plates are given through the best-performing gelatin composite of this study (4wt%). f) Ashby plot giving the compressive strength versus the density of the starch, agar, and gelatin composites and comparing it with other materials. The guidelines for minimum weight design of strong beams and of strong plates are given through the best-performing gelatin composite of this study (6 wt%).

and for MFC:G, a stiffness of 2 616.0 MPa and a strength of 93.07 MPa were found.

The sensors were printed on a low-roughness electronics paper substrate and were used as a sensing skin. This skin was bonded to the stiff and strong cryogel cores of the two wing sections and the fuselage section, resulting in a sandwich-structured composite. To evaluate the strengthening effect of the skin bonding, three-point bending tests were conducted using a mechanical testing machine (Z005 AllroundLine, ZwickRoell GmbH & Co. KG, Ulm, Germany) in combination

© 2023 The Authors. Advanced Intelligent Systems published by Wiley-VCH GmbH

26404567, 2023, 7, Downloaded from https://onlinelibrary.wiley.com/doi/10.1002/aisy.202300037 by Imperial College London, Wiley Online Library on [02/08/2023]. See the Terms and Conditions (https://onlinelibrary.wiley.com/terms-and-conditions) on Wiley Online Library for rules of use; OA articles are governed by the applicable Creative Commons License

with a 1 kN load-cell and an adjustable three-point bending setup made from steel. For calculating the flexural stiffness E_B, as well as the flexural strength σ_{fM}, the tests were performed on the basis of ASTM D790.[36] Nine 22 mm wide and 140 mm long samples were cut out of 6 wt% MFC:G plates using the CO_2 laser cutter operated at 75% power and 30 mm s^{-1} cutting speed. Using a 3D-printed grinding jig, the samples were ground to a nominal core thickness of 9 mm, which is the same height as the cord-root of the drone's wing. Afterward, the electronics paper was bonded on top and bottom of the foam core samples. The specimens were placed on the two supports ($R_1 = 5$ mm) of the three-point flexural rig at a support span length of 90 mm and the loading head ($R_2 = 5$ mm) was moved downward at a rate of 6 mm min^{-1}. To decrease the effect of introduced cover sheet buckling, 22 mm wide, 25 mm long, and 3 mm thick rubber pads with a Shore 60 A (Mold Max 60, Smooth-On Inc., Macungie, USA) were placed between the sample and the three loading positions. The flexural modulus as well as the strength were calculated following the guidelines given by ASTM D790. The individual sample masses were detected using a precision balance (Kern PCB 250-3, Kern & Sohn GmbH, Balingen-Frommern, Germany). It was found that the samples without face sheets had a mean flexural stiffness of $E_B = 4\,849$ MPa ($s = 706$ MPa) and a mean flexural strength of $\sigma_{fM} = 1.09$ MPa ($s = 0.25$ MPa), while the samples with face sheets achieved a mean flexural stiffness of $E_B = 13\,585$ MPa ($s = 2\,491$ MPa) and a mean flexural strength of $\sigma_{fM} = 2.15$ MPa ($s = 0.25$ MPa). Therefore, it was found that the flexural stiffness increased by a factor of 2.80×, and the flexural strength increased by a factor of 1.97× through the addition of the face sheets, while the weight increased by a factor of 1.31×.

The characterizations have shown that the mechanical properties of MFC:G composites are superior to the other binary compositions. It was found that the specific stiffness of MFC:G samples prepared from 4wt% slurries and the specific strength of MFC:G samples prepared from 6 wt% slurries outperform most other biodegradable, isotropic, and nonfossil foams discussed in the literature. Figure 4e summarizes this finding for the compressive modulus versus the material's density, while Figure 4f indicates the high compressive strength versus the material's density. Furthermore, the prepared starch and agar composites feature worse mechanical properties. Figure 4e indicates the performance indices for minimum weight design of the stiff beams and of the stiff plates through the 4 wt% MFC:G composite. Considering the slender wing as a beam-like structure and the square fuselage section as a plate, the indices can guide the material selection. To manufacture a stiff and lightweight structure, the wing section and the fuselage need to be manufactured from 4 wt% MFC:G cryogels. Figure 4f gives the performance indices for the minimum weight design of strong plates and strong beams. To design a strong and lightweight fuselage, the use of 6 wt% MFC:G would be favorable, while for a strong wing 8 wt% MFC:G would be optimal. According to these results, the wings and the fuselage were manufactured from 4 wt% MFC:G.

3.2. Microstructure

To estimate the homogeneity of the developed cryogels, the microstructure was investigated using SEM images and μ-CT scans. The SEM (Quanta 650 FEG ESEM, FEI, Hillsboro, Oregon, USA) images were taken at an accelerating voltage of 5 keV. For retrieving insights into the cross-sectional morphology, the cryogels were broken into two parts. Afterward, the samples were sputtered with 7 nm platinum (Bal-Tec MED 020 Modular High Vacuum Coating Systems, Bal-Tec AG, Liechtenstein). The resulting morphologies of the cryogels at a total weight content of 6 wt% (MFC:S, MFC:A, MFC:G) are shown in **Figure 5**a,e,i. To understand the volumetric morphology of the cryogels, their cell characteristics, and their pore size distributions, μ-CT (Easy Tom XL Ultra 230–160 micro/nano CT scanner, RX Solutions, Chavanod, France) scans were taken. The μ-CT scanner operated at 45kV and a current of 180 µA outputting a nominal resolution of 6 µm (voxel size). The samples were scanned full 360° with a continuous rotation acquiring 1568 projection with a frame average of four. Reconstruction of μ-CT slices was performed with dedicated software maintaining the same nominal resolution. A cubic volume of interest (VOI) of 5 mm per side was considered in each sample for the morphological analysis. The 2D slices were segmented and the detected pores were separated, computing the watershed lines using a chamfer matching algorithm. The distribution of pore size was calculated as equivalent diameter (Eq.D in µm). The separated 2D pores in each μ-tomographic section with a size of less than 17 µm (object of 2 × 2 pixels) were excluded to reduce noise. The 3D representation, the pore-size distribution histogram, as well as 2D cross-section views are given in Figure 5b–d,f–h,j–l. Videos indicating the porosity of each slice of the samples are provided in Movie S1, Supporting Information.

Starch is a polymeric carbohydrate consisting of two high molecular weight, polydisperse [1 → 4]-α-D-glucose polysaccharides: the highly branched amylose and the linear amylopectin.[37] Benefiting from its ability to associate into a range of semicrystalline forms, the starch polymers interweaved with MFC and formed aggregated structures during the process, leading to a porous structure. Agar is a mixture of small molecules, including β-D-galactose and 3, 6-lactone-L-galactose. During the freezing process, agar and MFC were consolidated and formed a structure with integrated large lamellas, as shown in Figure 5b. By contrast, the interweaved and cross-linked structures of MFC:S and MFC:G complexes cause their cryogels to demonstrate porous structures. Gelatin is a degradation of collagen, made of glycine, proline, and 4-hydroxy proline residues.[38] At temperatures above 40 °C, it has a random coil structure in solution,[39] and the formation of soluble MFC:G complexes via electrostatic attraction occurred. Once cooling below the coil-to-helix transition temperature of gelatin at around 4 °C, the polymers strongly intertwined with each other to form ordered triple-helical segments by hydrogen bonding.[40] At the same time, the gelatin-bridged MFC into a complex and a colocalized biopolymer network.[41] The great improvement of the mechanical strength of the MFC:G porous structure might indicate triple-helical segments forming during the freeze-drying.[42] Furthermore, its superior structural performance is in accordance with other reports illustrating that porcine gelatin films achieve almost two times higher strength than films fabricated from potato starch.[43,44]

© 2023 The Authors. Advanced Intelligent Systems published by Wiley-VCH GmbH

26404567, 2023, 7, Downloaded from https://onlinelibrary.wiley.com/doi/10.1002/aisy.202300037 by Imperial College London, Wiley Online Library on [02/08/2023]. See the Terms and Conditions (https://onlinelibrary.wiley.com/terms-and-conditions) on Wiley Online Library for rules of use; OA articles are governed by the applicable Creative Commons License

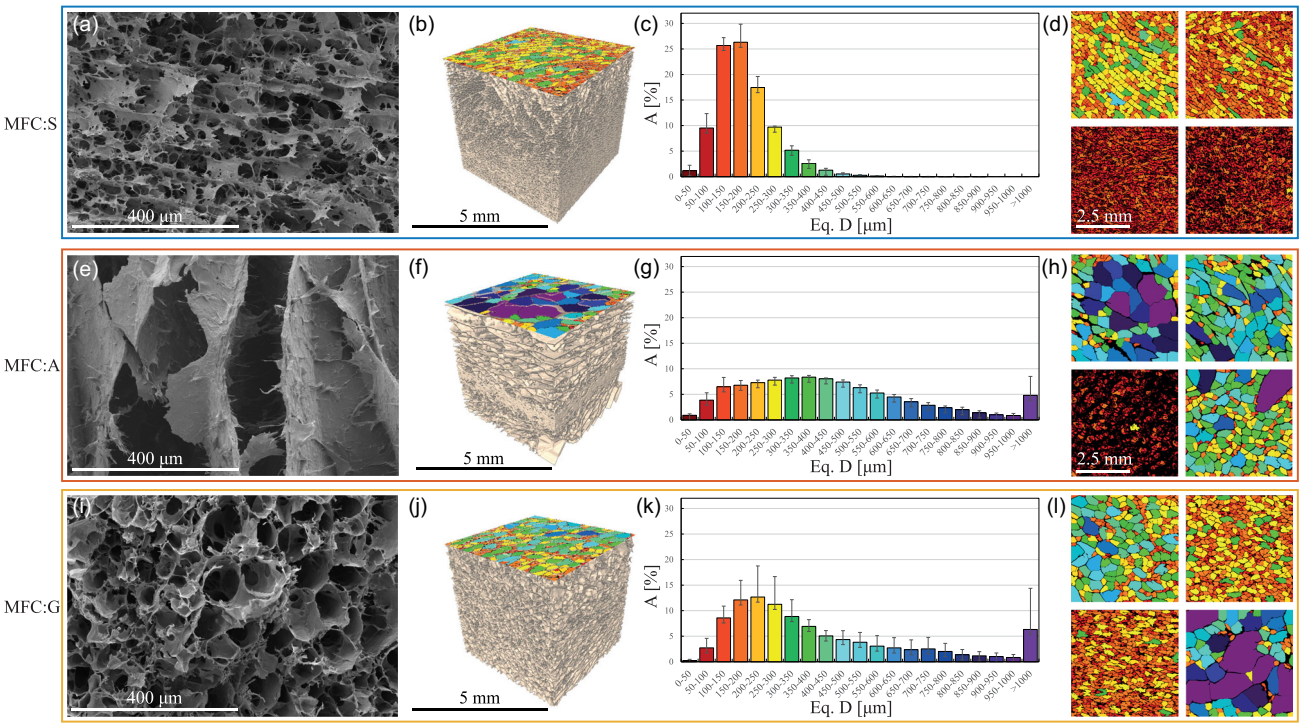

Figure 5. Overview of the cross-sectional morphology of the MFC:S, MFC:A, and MFC:G cryogel composites made from suspensions/solutions with a total weight content of 6%. The scanning electron microscope (SEM) images were generated at an accelerating voltage of 5 kV. The μ-computer tomography (μ-CT) scans were acquired with a X-ray source voltage of 45 kV. The colors correspond to the color-coded bars of the equivalent diameter ranges in µm. For visualization, 2D axial views of slices taken in the first, second, third, and fourth quarters of the VOI of the materials are given in the right column. a) Cross section of the total 6 wt% MFC:S cryogel at a magnification of 10 000×. b) The 3D model of a 125 mm^3 volume made from 6 wt% MFC:S. c) Histogram of the pore size distribution as area occupied in % grouped in different intervals of equivalent diameters of 6 wt% MFC:S. d) The 2D μ-CT slices of 6wt% MFC:S cryogels. e) Cross section of the total 6 wt% MFC:A cryogel at a magnification of 10 000×. f) 3D model of a 125mm^3 volume made from 6 wt% MFC:A. g) Histogram of the pore size distribution as area occupied in % grouped in different intervals of equivalent diameters of 6 wt% MFC:A. h) The 2D μ-CT slices of 6 wt% MFC:A cryogels. i) Cross section of the total 6 wt% MFC:G cryogel at a magnification of 10 000×. j) The 3D model of a 125 mm^3 volume made from 6 wt% MFC:G. k) Histogram of the pore size distribution as area occupied in % grouped in different intervals of equivalent diameters of 6 wt% MFC:G. l) The 2D μ-CT slices of 6 wt% MFC:G cryogels.

3.3. Biodegradation

For evaluating the degradation rate of the developed material system and the sensing skin, biodegradation tests of the investigated cryogel composites under accelerated conditions were performed. Conducting laboratory-scale tests to evaluate the disintegration rate under simulated aerobic composting conditions, the norm ISO 20200 was followed. The tests were performed for 70 days at constant 58 °C. The soil simulator was composed of sawdust, rabbit feed, cornstarch, sugar, corn oil, urea, and compost. The samples were put inside a protective mesh made from polypropylene and buried entirely in the soil. The mass of the sample was then weighed with and without the protective mesh in week 0–10, excluding week 9. The weight loss, as well as representative pictures of each sample at week 0, 1, 2, 3, and 10, is summarized in **Figure 6**.

It was found that the MFC:S and MFC:G samples degrade at a faster rate than the MFC:A samples. This is due to the more favorable chemical composition of starch and gelatin making it more susceptible to biodegradation by microorganisms. In general, the glucose units of starch and amino acids of gelatin can be more easily metabolized by microorganisms. Additionally, the water solubility of both biopolymers increases their biodegradation rate. Agar's stable polysaccharide structure, decreased nutritional source, and limited water solubility at the investigated temperature of 58 °C makes it more resistant to degradation. The found data is in line with other studies[45] reporting slower degradation rates of agar.

In accordance with the mechanical properties found, MFC:G in particular combines fast degradation and high mechanical properties and is therefore the most suitable candidate for manufacturing a lightweight, transient drone. Due to the lower temperatures present in the natural environments, the drone is designed to operate in, slower biodegradation rates of the airframe are expected. Furthermore, the changing environmental conditions in a natural setting might further affect the time period until full disintegration is achieved.

3.4. Sensing Characteristics

To quantify the capabilities of the proposed low-cost sensors, the bending sensor as well as the temperature sensors were tested

© 2023 The Authors. Advanced Intelligent Systems published by Wiley-VCH GmbH

26404567, 2023, 7, Downloaded from https://onlinelibrary.wiley.com/doi/10.1002/aisy.202300037 by Imperial College London, Wiley Online Library on [02/08/2023]. See the Terms and Conditions (https://onlinelibrary.wiley.com/terms-and-conditions) on Wiley Online Library for rules of use; OA articles are governed by the applicable Creative Commons License

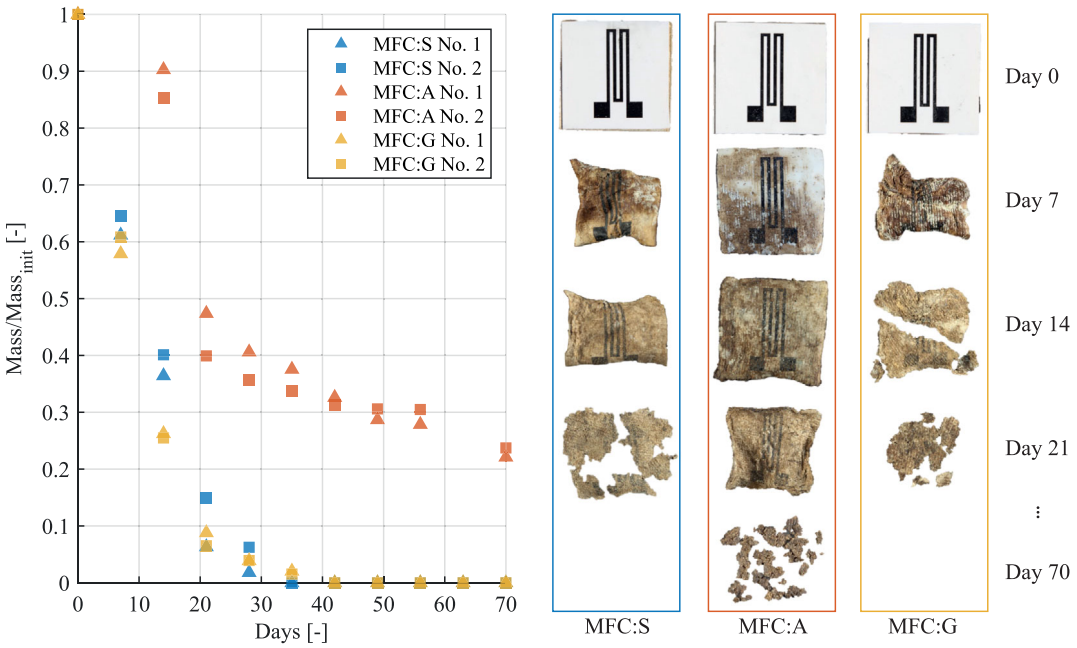

Figure 6. The weight loss of the investigated composites with bonded sensing skin. For week 0, 1, 2, 3, and 10, an image of a sample is given. The MFC:S and MFC: G samples have reached full disintegration after 5 and 6 weeks, respectively.

independently before integration into the eco-drone. For the characterization of the proprioception, a mock-up wing section was manufactured from 6wt% MFC:G cryogel. The electronics paper featuring a bending sensor was bonded to the wing section and the wing was clamped with a 3D-printed mount as seen in **Figure 7**a. After the installation of the servo motor and the rudder horn, the elevon was displaced, while the resistance of the sensor was continuously measured using a desktop multimeter (DMM6500 Desktop multimeter, Tektronix Inc., Beaverton, USA). First, the elevon was periodically displaced from −30° to 30° at a frequency of 1 Hz. Afterward, a step-wise deflection was induced ranging from −30° to 30° at a 10° step size. Each deflection was held for 60 s. Figure 7a shows the used testing setup and Figure 7b,c indicates the relative resistance change during the cyclic testing. Figure 7d indicates the relation between the deflection of the elevon and the corresponding relative resistance change. To characterize the exteroception capabilities of the proposed design, the temperature sensor was either not further treated or dip coated with carnauba- or beeswax. Afterward, the three sensors were connected to a data acquisition system (34970A, Agilent Technologies Inc., Santa Clara, USA) measuring the resistance change in a two-probe setup. The sensor was placed in a climatic chamber (Vötsch VC4100, Weiss Technik GmbH, Balingen, Germany) to create the desired temperature profile. The temperatures tested range from 15 to 35 °C at a constant relative humidity of 50% and each temperature was held for 2 h. For each temperature step, the average was computed and a scatter plot relating the temperature and the relative resistance change during the third cycle is shown in Figure 7e. To further understand the effect of humidity on the sensor and determine the best coating for the wing-integrated temperature sensor, tests have been conducted and the results are given in Figure S2a and S2b given in Section 1.2.2 in Supporting Information. Figure S2, Supporting Information, summarizes the third cycle relative resistance change depending on the relative humidity in the range of 10%–90% at constant 20°, while Figure S2b, Supporting Information, summarizes the relative resistance change taken in the range of 15–35 °C at a constant absolute humidity of 5.7 g cm^{-3}. Additionally, dynamic vapor sorption (DVS) tests were conducted using a bench-top DVS analyzer (Endeavour, Surface Measurement Systems Ltd., London, UK). The relative humidity was changed from 0% to 90% at a constant temperature of 20 °C. One untreated paper sample, one carnauba-wax and beeswax-coated sample as well as one carnauba-wax-coated sample with a printed resistor and one beeswax-coated sample with a printed resistor were analyzed. The results, which are summarized in Supporting Information Section 1.2.3 in Figure S3, indicate that the coatings limit the mass uptake, with beeswax performing the best. The data shows that the samples including a resistor feature a higher mass uptake than the blank samples.

The integrated bending sensors showed that changes in the elevon's deflection at a resolution of at least 10° were detectable, while indicating only minor hysteresis. In addition, the cyclic tests showed that the system had minor drift and performed well over the time tested. The integrated temperature sensor's performance is highly dependent on the coating used. While carbon features a negative temperature coefficient, a linear negative trend is observed when plotting the relative resistance change. The flat curve indicates rather low sensitivity to temperature changes, while a clear linear relationship is exhibited and no hysteresis is observed. The sensors coated in beeswax and carnauba-wax showed up to 19.12× and 11.45× higher sensitivity, respectively. Due to the penetration of the ink and paper with

© 2023 The Authors. Advanced Intelligent Systems published by Wiley-VCH GmbH

26404567, 2023, 7, Downloaded from https://onlinelibrary.wiley.com/doi/10.1002/aisy.202300037 by Imperial College London, Wiley Online Library on [02/08/2023]. See the Terms and Conditions (https://onlinelibrary.wiley.com/terms-and-conditions) on Wiley Online Library for rules of use; OA articles are governed by the applicable Creative Commons License

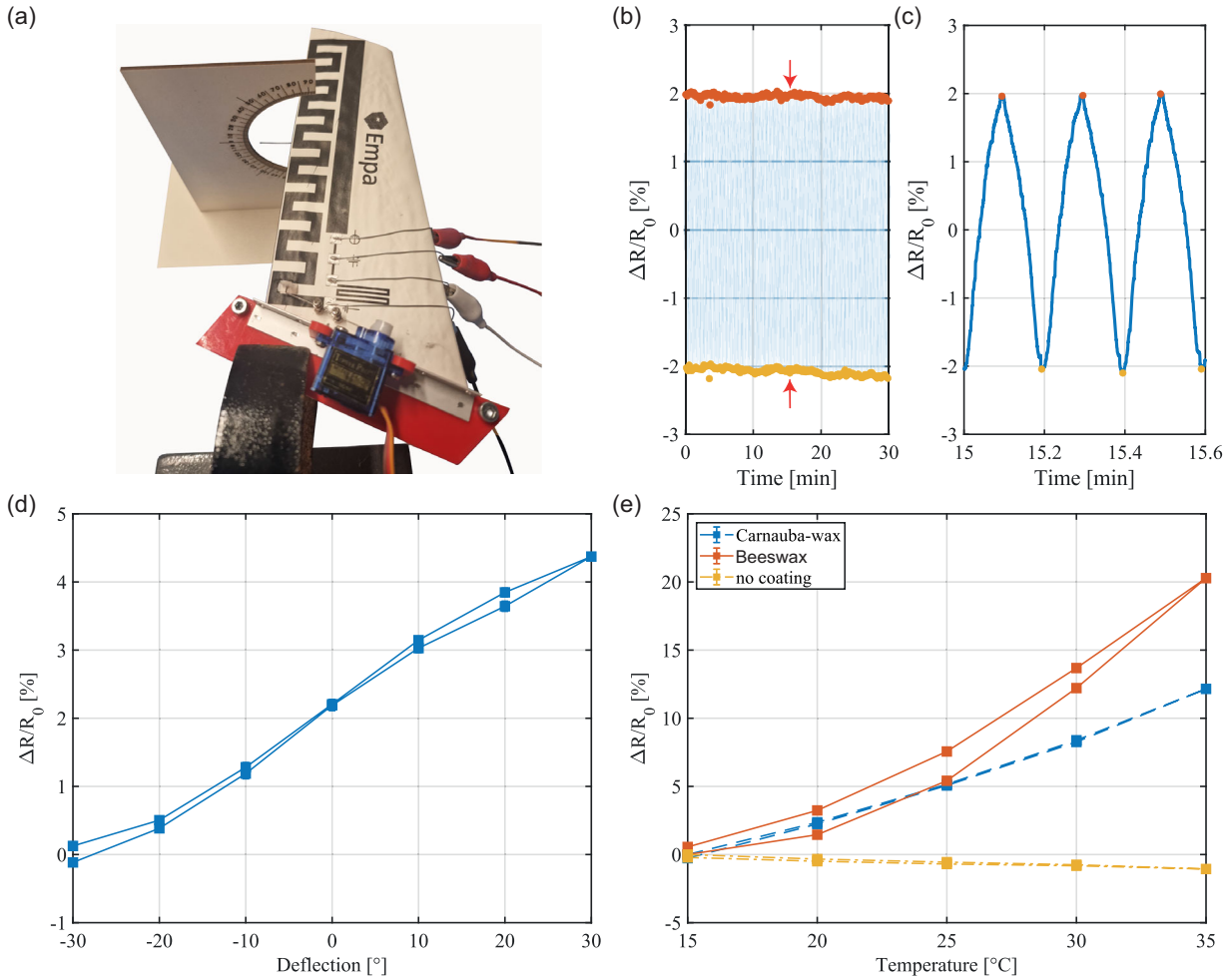

Figure 7. Sensing capabilities of the proposed drone. a) Flying wing section with integrated sensors clamped for proprioception characterization. b) Normalized, relative resistance change for 150 cycles changing the deflection from −30° to 30° at a frequency of 0.08 Hz. Each cycle's maximum and minimum are highlighted in red and yellow, respectively. c) Zoomed-in view of the normalized, relative resistance change at 15 min. d) Normalized, relative resistance change of the deflection sensor. The elevon angle was adjusted from −30° to 30° in 5° steps. Each angle was held for 60 s and the measured average was plotted. e) Normalized, relative resistance change of the printed temperature sensor versus ambient temperature ranging from 15 to 35 °C in 5 °C steps. The temperature sensor coated in carnauba-wax and beeswax and without coating has been investigated at a constant relative humidity of 50%, while each temperature plateau has been held constant for 2 h.

wax, which generally features a high coefficient of thermal expansion (CTE), the carbon-conductive ink itself expands when heated. This induces larger distances between the conductive particles in the ink and ultimately results in an increase in resistance. Therefore, the sensitivity difference between the used beeswax and carnauba-wax-coated sensors is due to the 2.2× higher CTE of carnauba-wax.[46] While the carnauba-wax-coated sensor features a linear relationship between relative resistance change and temperature as well as no visible hysteresis, the beeswax-coated sensor suffers from some nonlinearity as well as hysteresis, resulting in a relative resistance difference of up to 39.7% at 25 °C. This behavior is due to the lower melting point of beeswax. Nevertheless, the coated sensors are capable of measuring temperature down to a resolution of at least 5 °C. The information presented in Figure S2 in Section 1.2.2 in Supporting Information indicates that the carnauba-wax coating fails to mitigate resistance changes induced by changing relative humidity. In contrast, the measured resistance of the beeswax-coated sensor does not change up to a relative humidity of 80%. Therefore, it can be said that the beeswax-coated temperature sensor decouples the humidity-induced effect better and has a superior performance.

3.5. Flying Wing Testing

A 410 mm wingspan flying wing with an MH44 airfoil was manufactured using 4 wt% MFC:G. All the other components (vertical stabilizers, rudder horns, 3 inch diameter propeller, and electronics) were printed using a biodegradable polyhydroxybutyrate 3D-printing filament (AllPHA Natural, Colorfabb B.V., Belfeld, Netherlands). The electronics housing is used as a crash box containing all nondegradable components, such as a combined flight controller and electronic speed controller

© 2023 The Authors. Advanced Intelligent Systems published by Wiley-VCH GmbH

26404567, 2023, 7, Downloaded from https://onlinelibrary.wiley.com/doi/10.1002/aisy.202300037 by Imperial College London, Wiley Online Library on [02/08/2023]. See the Terms and Conditions (https://onlinelibrary.wiley.com/terms-and-conditions) on Wiley Online Library for rules of use; OA articles are governed by the applicable Creative Commons License

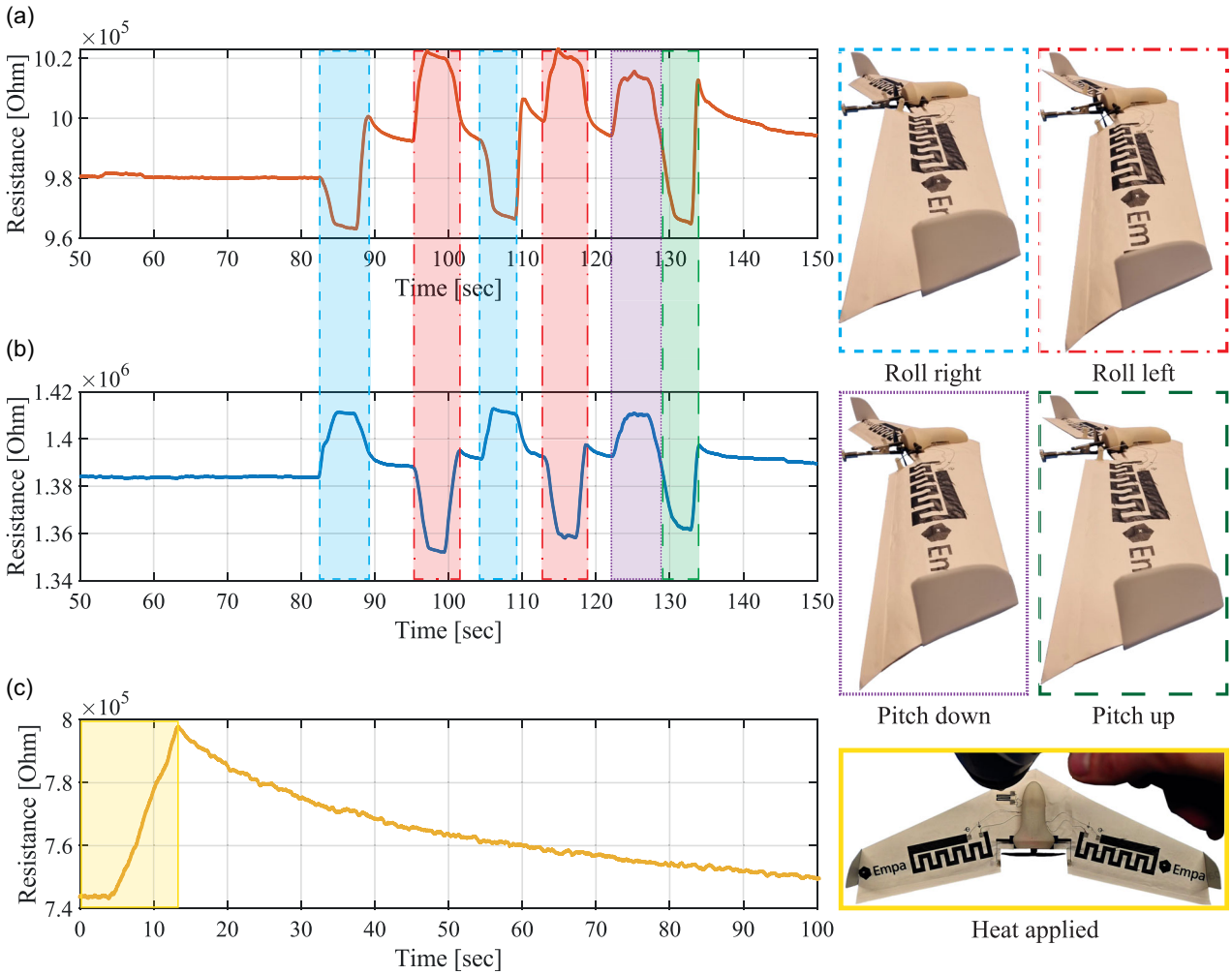

Figure 8. Testing of the integrated drone prototype. a) Post-processed signal of the right wing's sensing skin, during rolling to the right and left as well as pitching down and up. b) Post-processed signal of the left wing's sensing skin, during rolling to the right and left as well as pitching down and up. c) Transmitted resistance of the temperature sensors, when heated with a heat gun.

(MA-RX42-D+, OverskyRC Co. Ltd., Wuhan, China), two 1.7 × g servos for elevon actuation, a 100 mAh battery, a 16 000 Kv brushed motor, as well as the custom sensor terminal printed circuit board (PCB), featuring a Bluetooth transmission module. The printed sensors were connected to the sensor terminal PCB using zinc wires (zinc wire, Thermo Fisher Scientific Inc., Waltham, USA). While the deflection sensor reading was acquired using a Wheatstone bridge setup, the temperature sensor was analyzed utilizing a voltage divider. During testing, the control surfaces were remotely deflected, and the sensor terminal transmitted the voltage readings using Bluetooth to a ground station at a sampling frequency of 200 Hz. The received voltage was converted to the respective resistance reading and plots are given in **Figure 8**a,b for the right and left wings. Prior to plotting, a moving average filter with a window size of 100 readings was deployed. When a heat gun was pointed at the beeswax-coated temperature sensor, an increase in resistance was visible. The measured signal after filtering is shown in Figure 8c. A total resistance change of 54 kΩ was detected, which corresponds to a relative resistance change of 7.27%. Using the data presented in Figure 7e as a calibration curve, a local temperature increase of 9.66 °C was measured.

Range tests have shown that the data can be transmitted up to a range of 85 m, making the systems capable of medium-range environmental sensing flights. Further details on the design and manufacturing of the drone as well as the sensor terminal PCB are given in Supporting Information in Section 1.1.1, 1.2.4, and 1.1.2, respectively. A video of the lab-bench test conducted can be found in Movie S2, Supporting Information, while outdoor flight tests of the developed cryogel drone are provided in Movie S3, Supporting Information.

4. Conclusion

In this work, we have described manufacturing methods for generating lightweight and biodegradable structures through lyophilization, and proposed a material design and manufacturing

© 2023 The Authors. Advanced Intelligent Systems published by Wiley-VCH GmbH

26404567, 2023, 7, Downloaded from https://onlinelibrary.wiley.com/doi/10.1002/aisy.202300037 by Imperial College London, Wiley Online Library on [02/08/2023]. See the Terms and Conditions (https://onlinelibrary.wiley.com/terms-and-conditions) on Wiley Online Library for rules of use; OA articles are governed by the applicable Creative Commons License

process for transient aerial drones. It was found that MFC and gelatin composites feature superior mechanical properties over the here-tested biopolymer composite mixtures. Using this proposed manufacturing technique, more complex geometries were molded and structurally efficient structures with only a few grams of solid matter were fabricated. The material's capabilities were showcased through the manufacturing of a lightweight flying wing drone, designed for environmental monitoring. Through the integration of low-cost inkjet printed eco-friendly sensors, self-sensing and temperature-sensing skin was manufactured and integrated into the proposed transient drone design. The integrated sensors showed good performance in measuring the bending angle of the elevons, while the temperature sensor was capable of estimating the ambient temperature. Furthermore, it was shown that the chosen materials feature quick biodegradation and can be used for one-way missions in sensitive environments. The test flight showed that the proposed design achieves high agility while enabling efficient monitoring flights. Overall tools were presented that can be used to manufacture the next generation of lightweight transient drones with integrated proprioception and environmental sensing capability.

To extend the transient drone concept, further efforts should focus on the miniaturization of the required conventional electronics and the development of fully biodegradable components. The next steps could be the integration of biodegradable elevon actuators or the use of zinc-air-based batteries.[47] Additionally, materials other than carbon particles could be explored to realize resistive sensors.[48] For example, zinc- or magnesium-based ink could reduce the environmental impact of the sensors, while achieving higher conductivity. Especially, the lower resistivity renders the manufacturing of transient antennas[49] possible, which enables wireless transmission of environmental data. To reduce the amount of nondegradable components required, current developments in the field of transient electronics will need to directly feed into the transient drone design. The latest developments will enable environmental monitoring drones to be fully biodegradable and therefore enable environmental sensing one-way missions. While various approaches toward manufacturing and material selection are discussed in literature,[50,51] especially the development of transient transistors[52,53] will allow higher levels of autonomy for the drone. Nevertheless, the herein-developed platform can be used to carry various transient sensing devices, such as humidity or UV–intensity sensors. Overall, cryogel lyophilization results in lightweight and mechanically beneficial structures but requires a comparable high energy consumption. To further decrease the ecological footprint of the proposed transient robot, other less energy-intensive foam manufacturing techniques need to be investigated in the future.

Supporting Information

Supporting Information is available from the Wiley Online Library or from the author.

Acknowledgements

The authors thank Anja Huch for preparing the SEM images and Roman Elsener for providing his expertise in using the mechanical testing machine. Furthermore, the authors would like to thank Katrin Hoffmann for the preparation of the MFC, Yusuf Furkan Kaya for contributing the conceptual illustration, David Häusermann for the engineering support, Carolina Reyes for helping with the biodegradation test data interpretation, Max Widmer for piloting the drone as well as Roger Vonbank, and Bruno Binder and Ivan Lunati for experimental support and fruitful discussions. They also thank Luis Nicklaus Caceres and Claudio Sommer for soldering the sensor terminal PCBs. This work was supported in part by EPSRC Awards (grant nos. EP/R009953/1, EP/L016230/1, and EP/R026173/1), in part by NERC Award (grant no. NE/R012229/1), in part by the EU H2020 AeroTwin project under grant no. ID 810321, in part by the Royal Society Wolfson fellowship (grant no. RSWF/R1/18003), and in part by the Empa-Imperial research partnership.

Conflict of Interest

The authors declare no conflict of interest.

Data Availability Statement

The data that support the findings of this study are available from the corresponding author upon reasonable request.

Keywords

bio-hybrid materials, cryogel, environmental monitoring, flying wing, robotics, structural health monitoring, transient electronics

Received: January 18, 2023
Revised: March 24, 2023
Published online: April 27, 2023

[1] R. Cavicchioli, W. J. Ripple, K. N. Timmis, F. Azam, L. R. Bakken, M. Baylis, M. J. Behrenfeld, A. Boetius, P. W. Boyd, A. T. Classen, T. W. Crowther, R. Danovaro, C. M. Foreman, J. Huisman, D. A. Hutchins, J. K. Jansson, D. M. Karl, B. Koskella, D. B. Mark Welch, J. B. Martiny, M. A. Moran, V. J. Orphan, D. S. Reay, J. V. Remais, V. I. Rich, B. K. Singh, L. Y. Stein, F. J. Stewart, M. B. Sullivan, M. J. van Oppen, et al., *Nat. Rev. Microbiol.* **2019**, *17*, 569.
[2] FAO, UNEP, http://www.fao.org/documents/card/en/c/ca8642en (accessed: April 2023).
[3] W. L. Bauerle, J. D. Bowden, G. G. Wang, M. A. Shahba, *J. Exp. Bot.* **2009**, *60*, 3665.
[4] B. Tymen, G. Vincent, E. A. Courtois, J. Heurtebize, J. Dauzat, I. Marechaux, J. Chave, *Ann. For. Sci.* **2017**, *74*, 2.
[5] E. Naumburg, D. S. Ellsworth, *Oecologia* **2000**, *122*, 163.
[6] L. Mo, Y. He, Y. Liu, J. Zhao, S. J. Tang, X. Y. Li, G. Dai, in *Proc. of the 7th ACM Conf. on Embedded Networked Sensor Systems, SenSys 2009*, Berkeley, CA, 4–6 November **2009**, pp. 99–112, ISBN 9781605587486.
[7] E. Rödig, M. Cuntz, A. Rammig, R. Fischer, F. Taubert, A. Huth, *Environ. Res. Lett.* **2018**, *13*, 5.
[8] T. A. Ontl, M. K. Janowiak, C. W. Swanston, J. Daley, S. Handler, M. Cornett, S. Hagenbuch, C. Handrick, L. McCarthy, N. Patch, *J. For.* **2020**, *118*, 86.
[9] C. M. Figueiredo, E. F. Nakamura, A. D. Ribas, T. R. De Souza, R. S. Barreto, in *2009 2nd IFIP Wireless Days, WD 2009*, Paris, France, 15–17 December **2009**, ISBN 9781424456604.
[10] D. Debruyn, R. Zufferey, S. F. Armanini, C. Winston, A. Farinha, Y. Jin, M. Kovac, *IEEE Rob. Autom. Lett.* **2020**, *5*, 4564.

© 2023 The Authors. Advanced Intelligent Systems published by Wiley-VCH GmbH

26404567, 2023, 7, Downloaded from https://onlinelibrary.wiley.com/doi/10.1002/aisy.202300037 by Imperial College London, Wiley Online Library on [02/08/2023]. See the Terms and Conditions (https://onlinelibrary.wiley.com/terms-and-conditions) on Wiley Online Library for rules of use; OA articles are governed by the applicable Creative Commons License

[11] A. Farinha, R. Zufferey, P. Zheng, S. F. Armanini, M. Kovac, *IEEE Rob. Autom. Lett.* **2020**, *5*, 6623.
[12] F. Wiesemüller, Z. Meng, Y. Hu, A. Farinha, Y. Govdeli, P. H. Nguyen, G. Nyström, M. Kovač, *Front. Rob. AI* **2022**, *9*, https://doi.org/10.3389/frobt.2022.1011793.
[13] A. Heiden, D. Preninger, L. Lehner, M. Baumgartner, M. Drack, E. Woritzka, D. Schiller, R. Gerstmayr, F. Hartmann, M. Kaltenbrunner, *Sci. Rob.* **2022**, *7*, abk2119.
[14] F. Wiesemüller, A. Miriyev, M. Kovac, in *IEEE AIRPHARO 2021: The 1st AIRPHARO Workshop on Aerial Robotic Systems Physically Interacting with the Environment*, IEEE, Biograd na Moru, Croatia, 4 and 5 October **2021**, pp. 1–6.
[15] S. S. Sethi, M. Kovac, F. Wiesemüller, A. Miriyev, C. M. Boutry, *Nat. Ecol. Evol.* **2022**, *6*, 1245.
[16] J. Rossiter, J. Winfield, I. Ieropoulos, *Proceedings Volume 9798, Electroactive Polymer Actuators and Devices (EAPAD) 2016, SPIE Smart Structures and Materials + Nondestructive Evaluation and Health Monitoring*, Las Vegas, USA, 20–24 March **2016**.
[17] B. Mazzolai, C. Laschi, *Sci. Rob.* **2020**, *5*, aba6893.
[18] J. Shintake, H. Sonar, E. Piskarev, J. Paik, D. Floreano, in *2017 IEEE/RSJ Int. Conf. on Intelligent Robots and Systems (IROS)*, Vancouver, Canada, 24 September–1 October **2017**, pp. 6221–6226.
[19] A. Miriyev, M. Kovač, *Nat. Mach. Intell.* **2020**, *2*, 658.
[20] D. Feldmann, R. Das, B.-E. Pinchasik, *Adv. Mater. Interfaces* **2021**, *8*, 2001300.
[21] S. Ahankari, P. Paliwal, A. Subhedar, H. Kargarzadeh, *ACS Nano* **2021**, *15*, 3849, pMID: 33710860.
[22] J. Kim, S. Yun, Z. Ounaies, *Macromolecules* **2006**, *39*, 4202.
[23] T. Li, C. Chen, A. H. Brozena, J. Y. Zhu, L. Xu, C. Driemeier, J. Dai, O. J. Rojas, A. Isogai, L. Wågberg, L. Hu, *Nature* **2021**, *590*, 47.
[24] H. Sehaqui, M. Salajková, Q. Zhou, L. A. Berglund, *Soft Matter* **2010**, *6*, 1824.
[25] S. Zhao, W. J. Malfait, N. Guerrero-Alburquerque, M. M. Koebel, G. Nyström, *Angew. Chem., Int. Ed.* **2018**, *57*, 7580.
[26] J. Garemark, X. Yang, X. Sheng, O. Cheung, L. Sun, L. A. Berglund, Y. Li, *ACS Nano* **2020**, *14*, 7111, pMID: 32413254.
[27] N. Buchtová, C. Pradille, J.-L. Bouvard, T. Budtova, *Soft Matter* **2019**, *15*, 7901.
[28] Y. Kobayashi, T. Saito, A. Isogai, *Angew. Chem. Int. Ed.* **2014**, *53*, 10394.
[29] C. Lei, K. Wu, L. Wu, W. Liu, R. Du, F. Chen, Q. Fu, *J. Mater. Chem. A* **2019**, *7*, 19364.
[30] A. Liu, L. Medina, L. A. Berglund, *ACS Appl. Mater. Interfaces* **2017**, *9*, 6453.
[31] S. Josset, P. Orsolini, G. Siqueira, A. Tejado, P. Tingaut, T. Zimmermann, *Nordic Pulp Pap. Res. J.* **2014**, *29*, 167.
[32] S. Josset, L. Hansen, P. Orsolini, M. Griffa, O. Kuzior, B. Weisse, T. Zimmermann, T. Geiger, *Cellulose* **2017**, *24*, 3825.
[33] C. Antonini, T. Wu, T. Zimmermann, A. Kherbeche, M. J. Thoraval, G. Nyström, T. Geiger, *Nanomaterials* **2019**, *9*, 1142.
[34] ASTM International, Technical Report, ASTM International **2016**.
[35] L. J. Gibson, M. F. Ashby, *Cellular Solids, Structure and Properties*, Cambridge University Press, Cambridge **1997**.
[36] ASTM International, Technical Report, **2020**.
[37] T. T. Koev, J. C. Muñoz-García, D. Iuga, Y. Z. Khimyak, F. J. Warren, *Carbohydr. Polym.* **2020**, *249*, 116834.
[38] K. Deshmukh, M. Basheer Ahamed, R. Deshmukh, S. Khadheer Pasha, P. Bhagat, K. Chidambaram, *Biopolymer Composites in Electronics*, Elsevier, Amsterdam **2017**, pp. 27–128.
[39] Q. He, H. Yan, S. Wang, *Adv. Funct. Mater.* **2018**, *28*, 1705069.
[40] M. Roussenova, J. Enrione, P. Diaz-Calderon, A. J. Taylor, J. Ubbink, M. A. Alam, *New J. Phys.* **2012**, *14*, 035016.
[41] C. S. Wang, N. Virgilio, P. M. Wood-Adams, M. C. Heuzey, *Food Hydrocolloids* **2018**, *79*, 462.
[42] S. Cai, Z. Sun, H. Wang, X. Yao, H. Ma, W. Jia, S. Wang, Z. Li, H. Shi, Z. An, Y. Ishida, T. Aida, W. Huang, *J. Am. Chem. Soc.* **2021**, *143*, 16256.
[43] A. Bigi, S. Panzavolta, K. Rubini, *Biomaterials* **2004**, *25*, 5675.
[44] S. P. Bangar, S. S. Purewal, M. Trif, S. Maqsood, M. Kumar, V. Manjunatha, A. V. Rusu, *Foods* **2021**, *10*, 2181.
[45] O. Dzeikala, M. Prochon, A. Marzec, S. Szczepanik, *Int. J. Mol. Sci.* **2023**, *24*, 1473.
[46] R. Craig, J. Eick, F. Peyton, *J. Dent. Res.* **1965**, *44*, 1308.
[47] A. Poulin, X. Aeby, G. Nyström, *Sci. Rep.* **2022**, *12*, 11919.
[48] X. Aeby, J. Bourely, A. Poulin, G. Siqueira, G. Nyström, D. Briand, *Adv. Mater. Technol.* **2022**, *8*, 2201302.
[49] Y. Sui, A. N. Radwan, A. Gopalakrishnan, K. Dikshit, C. J. Bruns, C. A. Zorman, G. L. Whiting, *Adv. Eng. Mater.* **2023**, *25*, 2200529.
[50] R. Jamshidi, M. Taghavimehr, Y. Chen, N. Hashemi, R. Montazami, *Adv. Sustainable Syst.* **2022**, *6*, 2100057.
[51] J. Li, J. Liu, W. Huo, J. Yu, X. Liu, M. Haslinger, M. Muehlberger, P. Kulha, X. Huang, *Mater. Today Nano* **2022**, *18*, 100201.
[52] M. Landers, A. Elhadad, M. Rezaie, S. Choi, *ACS Appl. Mater. Interfaces* **2022**, *14*, 45658, pMID: 36166404.
[53] M. Stephen, A. Nawaz, S. Y. Lee, P. Sonar, W. L. Leong, *Adv. Funct. Mater.* **2023**, *33*, 2208521.
[54] A. Lopez-Gil, F. Silva-Bellucci, D. Velasco, M. Ardanuy, M. A. Rodriguez-Perez, *Ind. Crops Prod.* **2015**, *66*, 194.
[55] A. J. Svagan, M. A. Samir, L. A. Berglund, *Adv. Mater.* **2008**, *20*, 1263.
[56] H. Sehaqui, Q. Zhou, L. A. Berglund, *Compos. Sci. Technol.* **2011**, *71*, 1593.
[57] A. E. Donius, A. Liu, L. A. Berglund, U. G. Wegst, *J. Mech. Behav. Biomed. Mater.* **2014**, *37*, 88.
[58] A. J. Svagan, L. A. Berglund, P. Jensen, *ACS Appl. Mater. Interfaces* **2011**, *3*, 1411.

© 2023 The Authors. Advanced Intelligent Systems published by Wiley-VCH GmbH

26404567, 2023, 7, Downloaded from https://onlinelibrary.wiley.com/doi/10.1002/aisy.202300037 by Imperial College London, Wiley Online Library on [02/08/2023]. See the Terms and Conditions (https://onlinelibrary.wiley.com/terms-and-conditions) on Wiley Online Library for rules of use; OA articles are governed by the applicable Creative Commons License